Surface self-reconstruction of telluride induced by in-situ cathodic electrochemical activation for enhanced water oxidation performance

Peng Guo [a], Shoufu Cao [b], Yijin Wang [a], Xiaoqing Lu [b], Youzi Zhang [a], Xu Xin [a], Xiao Chi [c], Xiaojiang Yu [d], Ilhom Tojiboyev [e], Hadi Salari [f], Ana Jorge Sobrido [g], Magdalena Titirici [h], Xuanhua Li [a],*

[a] *State Key Laboratory of Solidification Processing , Center for Nano Energy Materials , School of Materials Science and Engineering , Northwestern Polytechnical University , Xi'an 710072, China*
[b] *School of Materials Science and Engineering , China University of Petroleum (East China), Qingdao 266580, China*
[c] *Department of Physics, National University of Singapore 117576, Singapore*
[d] *Singapore Synchrotron Light Source, National University of Singapore, 5 Research Link, 117603, Singapore*
[e] *Institute Ion - Plasma and Laser Technologies, Uzbekistan Academy of Sciences, Durmon yuli 33, Tashkent 100125, Uzbekistan*
[f] *Faculty of Physical Chemistry, Shiraz University, Shiraz 71345, Iran*
[g] *Materials Research Institute, School of Engineering and Materials Science, Faculty of Science and Engineering, Queen Mary University of London, Mile End Road, London E1 4NS, UK*
[h] *Department of Chemical Engineering, Imperial College London, South Kensington Campus, London SW7 2AZ, United Kingdom*

ARTICLE INFO

ABSTRACT

Metal tellurides attract recent attention because of their promising applications as effective catalysts for the oxygen evolution reaction (OER). However, inappropriate adsorption energy between OER intermediates and telluride leads to an unsatisfactory electrocatalytic intrinsic activity. Herein, we adopt a unique in-situ cathodic electrochemical activation process to facilitate the surface self-reconstruction to form oxygen vacancy (O_V)-rich TeO_2 layer onto Fe-doped NiTe (O_V@Fe-NiTe). Characterizations and theoretical calculation demonstrate that the presence of the O_V-rich TeO_2 layer realizes the adjustment of D-band center of the active site that translates into an enhancement of the adsorption of *OOH intermediate and thus the optimization of the OER pathway. Consequently, the O_V@Fe-NiTe only requires an ultralow overpotential of 245 mV to drive 100 mA cm^{-2} in 1 M KOH, 95 mV lower than that of Fe-NiTe, and hence becoming the best water oxidation electrocatalysts amongst recently reported telluride electrocatalysts. This study presents a unique strategy to exploit telluride-based catalysts through electrochemical surface engineering.

1. Introduction

The oxygen evolution reaction (OER) has hindered the efficiency of important electrochemical energy conversion processes, including H_2 generation via water splitting, N_2 fixation and CO_2 reduction, on account of the sluggish kinetics [1–4]. Because of this, costly and scarce electrocatalysts, such as Ir and Ru-based compounds, are usually employed, making the development of new low-cost catalysts extremely urgent [5–8]. Owing to the outstanding catalytic performance and earth abundance, nano-sized chalcogenides have been considered as ideal replacement of the noble-based OER electrocatalysts [9–12]. Due to its better electric conductivity and band alignment compared with the other chalcogenides, the metal telluride has attracted much interest for OER electrocatalysis [13–16].

Effective strategies are reported to develop efficient telluride electrocatalysts for the water oxidation, such as interface engineering [17–19], crystallization state adjustment [20,21], carbon-modification [16,22,23] and phase-selection [14]. For example, Li.et constructs NiTe/NiS nanointerface to achieve OER property enhancement [17]. Regulating the local coordination environment of Te in $RuTe_2$ through an amorphous activation to optimize the OER pathway and facilitate the electron transfer in OER according to Huang's report [20]. Yu.et finds that cobalt telluride with $CoTe_2$ phase exhibit better OER performance than with CoTe phase [14]. However, inappropriate adsorption energy

between OER intermediates and telluride leads to an unsatisfactory electrocatalytic activity [24–27], which is still a bottleneck for the telluride electrocatalyst.

Herein, we adopt an in-situ cathodic electrochemical activation (CEA) process to achieve the self-reconstruction of Fe-doped NiTe (Fe-NiTe, see Fig. 1a). Chemical composition and electronic configuration characterizations confirm that the CEA process facilitates the formation of oxygen vacancy-rich (O_V-rich) TeO_2 layer on the surface of Fe-NiTe (O_V@Fe-NiTe, where O_V represents oxygen vacancy). The formed O_V-rich TeO_2 promotes the adjustment of the position of D-band center (ε_d) of tellurium, which in turn facilitates the formation of *OOH intermediate and thus, enhance the OER performance of O_V@Fe-NiTe. As a result, the OER overpotential is drastically decreased from 340 mV (Fe-NiTe) to 245 mV (O_V@Fe-NiTe) at current density of 100 mA cm^{-2} in 1 M KOH, and the O_V@Fe-NiTe also displays fast kinetics and excellent stability over 100 h. This strategy demonstrates that the unique surface self-reconstruction of telluride induced by the CEA process has positive effect on OER.

2. Experimental section

2.1. Preparation of Fe-Ni(OH)$_2$, Ni(OH)$_2$ precursor

0.5 mmol ferric nitrate ninhydrate, 1 mmol nickel nitrate hexahydrate, 10 mmol urea and 0.2 g ammonium fluoride were added into 30 mL deionized water and stirred for 10 min. The obtained solution and the Ni foam were transferred into a 50 mL autoclave. The hydrothermal setup was reacted at a temperature of 120 ℃ for 6 h. After the temperature decreased to room temperature, the obtained materials were washed by water and ethanol for several times and dried at 70 ℃ for 12 h. The Ni(OH)$_2$ was synsized using the same approach without Fe(NO$_3$)$_3 \bullet$9 H$_2$O.

2.2. Synthesis of Fe-NiTe, NiTe

2 mmol Na$_2$TeO$_3$ was dissolved into distilled water (20 mL) and stirred for 20 min. After that,10 mL N$_2$H$_4$ was added in the Na$_2$TeO$_3$ solution. Then, the mixed solution and the as-prepared Fe-Ni(OH)$_2$ precursor were added into a 50 mL autoclave. The hydrothermal reaction was conducted at a temperature of 180 ℃ for 24 h. The obtained material was cleaned by distilled water and dried at 70 ℃ for 12 h. The
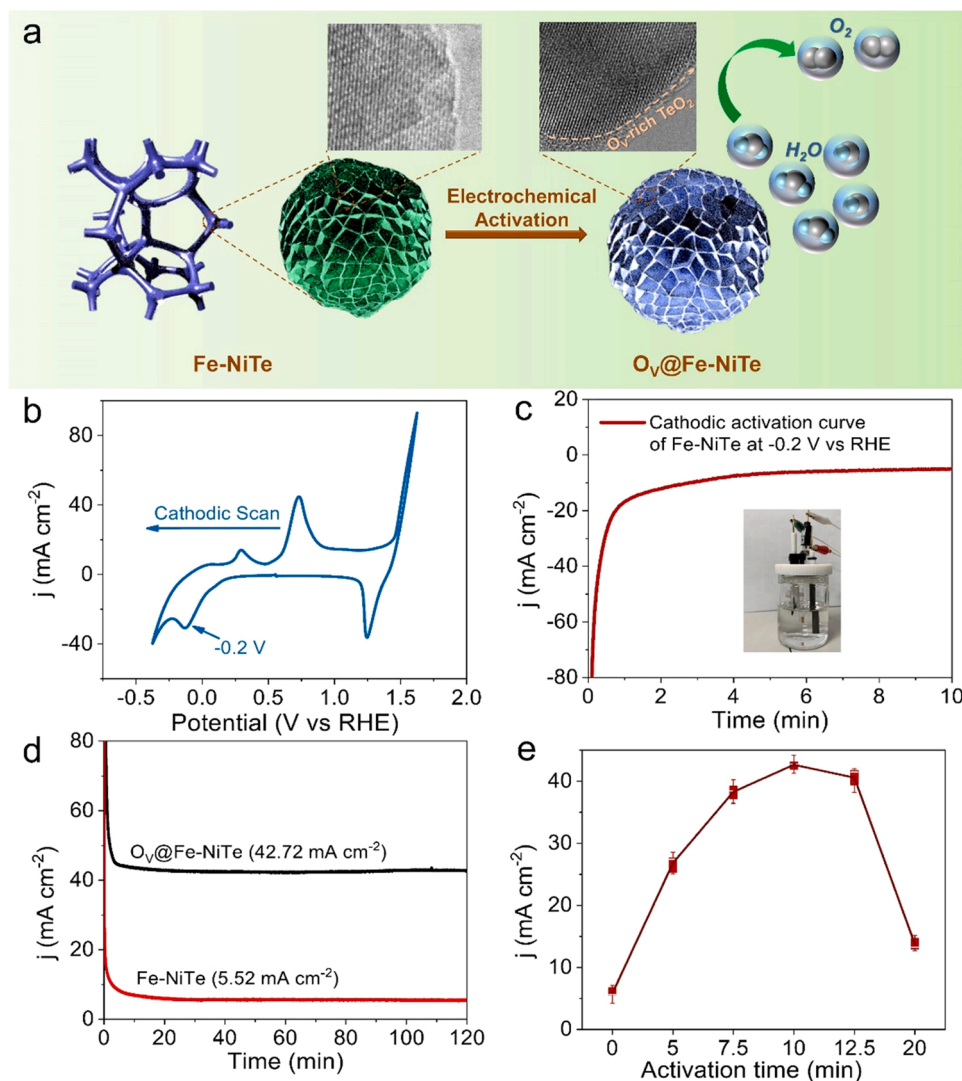
Fig. 1. (a) Schematic illustration of the formation of O_V@ Fe-NiTe. (b) Cathodic CV scan curves of the pristine Fe-NiTe. (c) Electrochemical activation i-t curves for the synthesis of O_V@Fe-NiTe. The inset presents the three-electrode activation set-up. (d) Chronoamperometric i-t curves of O_V@Fe-NiTe and Fe-NiTe (without iR correction) at 1.585 V. (e) Current density at 1.585 V vs RHE of Fe-NiTe at different electrochemical activation time.

NiTe were prepared using the $Ni(OH)_2$ as precursor in the same method.

2.3. Preparation of O_V@Fe-NiTe

The electrochemical activation of Fe-NiTe was conducted in 1 M KOH using a three-electrode system to obtain O_V@Fe-NiTe. The as-prepared material was working electrode, Hg/HgO was served as reference electrode and the carbon rod was served as counter electrode. The activation process was performed at − 0.2 V vs RHE (reversible hydrogen electrode) for 10 min

2.4. Preparation of pristine TeO_2

1 mmol Na_2TeO_3 was stirred in 25 mL deionized water for 20 min, and 1 mL acetic acid was added into the solution drop by drop. Then, the solution was aged for 1 h. The white production was collected via centrifugation and washed by deionized water. The obtained TeO_2 was dried at 70 ℃ for 12 h.

2.5. Characterization

The crystalline structure was characterized by XRD (X-ray diffraction, λ = 0.15418 nm). SEM (scanning electron microscope, FEI Nova-sem) and TEM (transmission electron scope, Tecnai F30G2) were performed to observe the morphology of materials. X-ray photoelectron spectra (XPS, Axis Supra) was conducted to characterize the composition on the surface of materials. Raman spectrometer (Renishaw inVia) was used to obtain the Raman spectra of the materials using the laser with a wave length of 532 nm. X-ray adsorption spectrum (XAS) characterizations of all the samples were conducted in the Singapore synchrotron light source on the BEAR beamline. The Inductively Coupled Plasma Optical Emission (ICP, ThermoFisher) was performed to characterize the ion concentration in the electrolyte.

2.6. Electrochemical measurement

All the electrochemical tests were conducted using a traditional three-electrode system in 1 M KOH on a CHI760E electrochemical workstation. The work electrode is the obtained materials, which wascut into a seize of 1 cm * 2 cm;the counter electrode is carbon dot; and the reference electrode is Hg/HgO electrode with 1 M KOH. The LSV (Linear sweep voltammetry) curves were recorded with iR correction at 5 mV s^{-1}. ECSA (electrochemical surface area) of the materials were acquired by recording CVs in the same potential window from 5 mV s^{-1} to 25 mV s^{-1}. EIS (electrochemical impedance spectroscopy) of samples were recorded at a frequency region of 0.01–10^5 Hz. The stability of the catalysts was evaluated by the chronoamperometry. The potential was calibrated to RHE using the following equation:

$$E(RHE) = 0.098 + 0.059 * pH + E(Hg/HgO) \qquad (1)$$

5 mg TeO_2 and commercial RuO_2 were dispersed in the mixed solvent of ethanol and water (v/v=1:1), respectively. Then, 30 μL 5 wt% Nafion solution was introduced in the TeO_2 and RuO_2 dispersion liquid and ultrasonicated for 30 min 5 μL uniform TeO_2 ink was coated on the glassy carbon electrode, and the CV curves of TeO_2 were recorded in a three-electrode configuration (the carbon rod and Hg/HgO electrode were served as counter electrode and reference electrode, respectively) with a scan rate of 10 mV s^{-1}. 200 uL uniform RuO_2 ink was coated on the Ni foam (1 *1 cm), the OER performance of RuO_2 was evaluated in the same method with the as-prepared catalysts.

2.7. Computational details

The plane-wave technique implemented in the Vienna Ab-initio Simulation Package (VASP) was used to perform all the DFT calculations [28]. A plane-wave cutoff energy was set to be 420 eV and the generalized gradient approximation expressed by Perdew-Burke-Ernzerh of functional were used in all DFT calculations [29]. The k-points and the k-points for electronic densities of states were set to $3 \times 3 \times 1$ and $11 \times 11 \times 1$, which were used for geometry optimization and accurate calculation, respectively. The convergence of energy was set to 1×10^{-5} eV and forces was set to 0.02 eV Å^{-1}. The van der Waals interactions were described using Dispersion correction (DFT-D3) proposed by Grimme. The VASP implicit solvent model was used to study the effect of water [30].

The CHE (computational hydrogen electrode) model was used to calculate the variation of Gibbs free energy [31]. The Gibbs energy can be obtained by taking zero- entropy corrections and point energy into consideration as follows:

$$\Delta G = \Delta E + \Delta E_{ZPE} - T\Delta S + \Delta G_U + \Delta G_{pH} \qquad (2)$$

in the above equation, ΔE is the reaction energy, ΔE_{ZPE} is t the difference in zero-point energy and entropy between the adsorbed species and free species. ΔG_U is set as 0 V, which is corresponding to applied potential (U) and ΔG. ΔG_{pH} is the free energy from the change of pH value.

The Oxygen evolution reaction (OER) free energy diagrams were calculated along the following four electrons reaction pathways:

$$H_2O(l) + * \rightarrow OH* + (H^+ + e^-) \qquad (3)$$

$$OH* \rightarrow O* + (H^+ + e^-) \qquad (4)$$

$$O* + H_2O(l) \rightarrow OOH* + (H^+ + e^-) \qquad (5)$$

$$OOH* \rightarrow * + O_2(g) + (H^+ + e^-) \qquad (6)$$

where the * represents active site on the surface of the catalyst, l is the liquid phase of H_2O, g is the gas phase of O_2. The O*, OH*, and OOH* represent intermediate coordination of O$^-$, OH$^-$, and OOH$^-$ adsorbed at active sites, respectively.

3. Results and discussion

3.1. Synthesis and characterization

Fe-NiTe was firstly synthesized in a facile anion exchange method using $Ni(OH)_2$ and $Fe-Ni(OH)_2$ nanosphere as precursor and Na_2TeO_3 as tellurium source. Through the structural characterization and electro-catalytic performance measurements (Fig. S1-6, details in supplementary materials) demonstrate that Fe dopes into the NiTe can effectively enhance the electrocatalytic activity through providing abundant active sites and facilitating the electron transfer. Subsequently, we adopted a novel cathodic electrochemical activation process (i.e., CEA) to induce oxygen vacancies in the TeO_2 formed at the surface of the telluride (Fig. 1a and experimental section). We conducted cathodic cyclic voltammetry measurements to pristine Fe-NiTe. As shown in Fig. 1b, a clear peak at − 0.2 V vs RHE is observed, which is corresponding to the electroreduction of formed TeO_2 on the Fe-NiTe according to the CV cathodic curve of pristine TeO_2 (Fig. S7) and previous report [32]. This phenomenon indicates the electrochemical activation is an efficient strategy to regulate the surface self-construction of the telluride. Encouraged by this observation, we carried out the activation of Fe-NiTe through a unique CEA process via applying a sustainable bias of − 0.2 V vs RHE during 10 min, as displayed in Fig. 1c. We recorded the i-t curves for both pristine Fe-NiTe and O_V@Fe-NiTe at 1.585 V vs RHE (Fig. 1d). Interestingly, we detected a sustained current density of 42.72 mA cm^{-2} for O_V@Fe-NiTe, about 8 times higher than that observed for pristine Fe-NiTe (5.52 mA cm^{-2}) under the same experimental conditions. To obtain the optimal activation time, we performed a series of experiments at − 0.2 V using different activation times. The result suggested that the optimal activation time that could deliver the highest current density was 10 min (Fig. 1e and S8). On the contrary, no evident increasing of the current density for Fe-NiTe at a continuous bias of 1.585 V is

detected (Fig. 1d), which suggests that the anodic activation could not improve OER property.

We investigated the O_V@Fe-NiTe morphology and TeO_2 formed at the surface of the telluride. As shown in Fig. 2a-c, the O_V@Fe-NiTe is composed of microspheres with a diameter of 5 μm, which is similar to the structure of pristine Fe-NiTe (Fig. S3a and b). Fig. 2d and e further suggest that the O_V@Fe-NiTe microsphere is composed of nanosheet with a width about 200 nm. Different from the pristine Fe-NiTe (see Fig. S3d), the O_V@Fe-NiTe microsphere formed a more obvious TeO_2 layer with a thickness of ~2 nm (Fig. 2f), suggesting that CEA process could indeed facilitate the surface reconstruction of pristine Fe-NiTe. The lattice spacing of 2.8 Å of the O_V@Fe-NiTe (Fig. 2f) corresponds to the (101) plane of the hexagonal Fe-doped NiTe [23], which is consistent with that of pristine Fe-NiTe (Fig. S3d). Fig. 2g~k confirm that Ni, Fe, Te and O uniformly distribute in O_V@Fe-NiTe.

We further investigated the chemical states of the formed TeO_2 formed on the O_V@Fe-NiTe (Fig. 3b-f). XRD patterns of O_V@Fe-NiTe and pristine Fe-NiTe (Fig. 3a) shows a crystalline phase corresponding to NiTe and Ni (corresponding to the Ni foam), which suggests that the CEA process does not change the crystalline structure of O_V@Fe-NiTe significantly. Fig. 3b shows the Raman spectra of O_V@Fe-NiTe and pristine Fe-NiTe, where the peaks at $100 \sim 200$ cm^{-1} are assigned with the telluride, while the peaks in $600 \sim 800$ cm^{-1} correspond to the TeO_2 layer [33,34]. In detail, the peaks at $550 \sim 700$ cm^{-1} correspond to the asymmetric Te−O−Te bridge between $[TeO_4]$ units, the peaks locate at $700 \sim 800$ cm^{-1} arise from the continuous $[TeO_4]$ network in the formed TeO_2 layer [35,36]. In the high resolution XPS Te 3d spectra in Fig. 3c,

no evident peaks correspond to the M-Te bond (M=Ni, Fe) around 583.37 eV and 572.97 eV in the O_V@Fe-NiTe. According to the previous reports, the evident decrease of M-Te peaks suggests that the substance transformation occurs on the surface of Fe-NiTe. [37]. The peaks at 586.57 eV and 581.17 eV of Fe-NiTe are corresponding to the Te^{4+} from the TeO_2 [16,38]. The increasing of Te-O peaks further demonstrate that the substance transformation is the formation of TeO_2 layer. Interestingly, the peaks related to the tellurium oxide of the OV@Fe-NiTe is at 586.27 eV and 575.87 eV. The peaks of the OV@Fe-NiTe are obviously negative shift compared with that of the pristine Fe-NiTe, which suggests that the generation of oxygen vacancy in the TeO_2 layer after the CEA process. The deconvoluted peaks at 530.5, 531.4, 532.2, 533.2 eV are related to lattice O, surface O, oxygen vacancy (O_V) and the adsorbed H_2O, respectively in the O 1 s spectra of the O_V@Fe-NiTe and pristine Fe-NiTe (Fig. 3d) [5,26,27,39–43]. The higher content of oxygen vacancy in the O_V@Fe-NiTe also supports the formation of O_V-rich TeO_2.

To further prove the formation of O_V-rich TeO_2 on the surface of O_V@Fe-NiTe, we characterized the fine structure of O_V@Fe-NiTe and pristine Fe-NiTe using X-ray adsorption spectrum (XAS). Fig. 3e presents the XAS Te $M_{2,3}$-edge spectrum of O_V@Fe-NiTe and pristine Fe-NiTe. Both spectra showed similar features. The peaks located at around 577.8 eV and 587.6 eV are related to the splitting of Te $3p_{3/2}$-$3p_{1/2}$ spin-orbital. There is an evident positive shift of photo energy of O_V@Fe-NiTe with respect to pristine Fe-NiTe, suggesting an increase of active Te as a consequence of the formation of the O_V-rich TeO_2 layer. In combination with the above XPS characterization, the formed TeO_2 layer on the O_V@Fe-NiTe contains Te with lower oxidation state compared with the
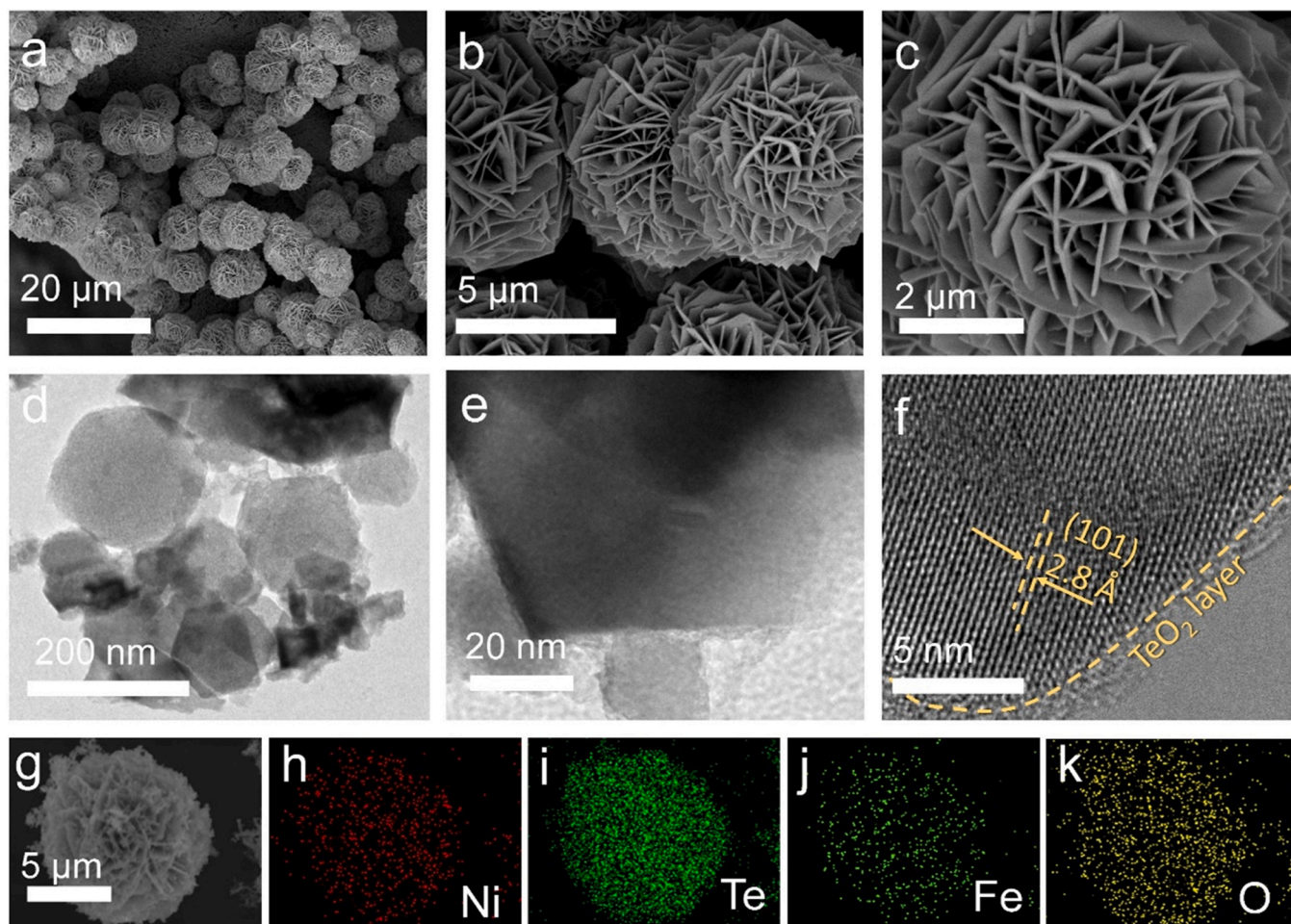
Fig. 2. (a)~(c) Different resolution SEM images of O_V@Fe-NiTe. (d) TEM and (e) (f) HRTEM images of O_V@Fe-NiTe. (g) SEM image and (h)~(f) corresponding element mappings of O_V@Fe-NiTe.
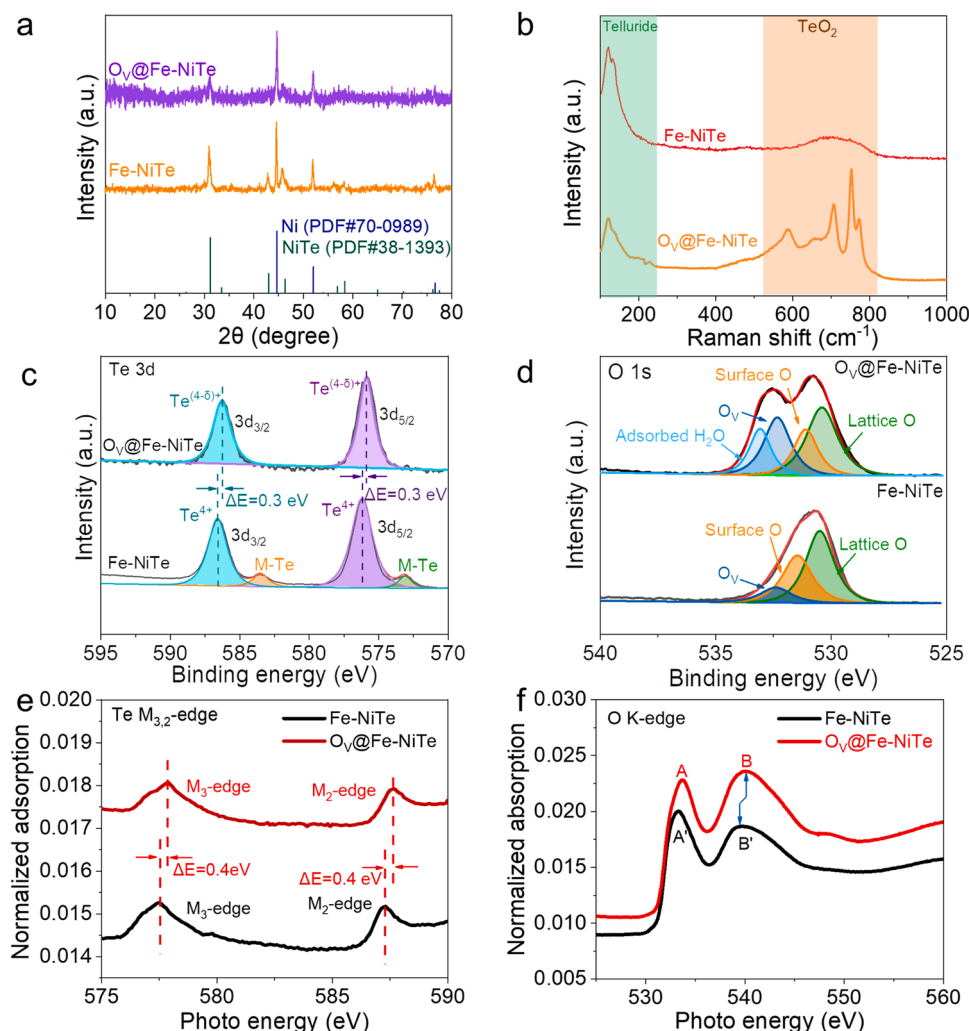
Fig. 3. (a) XRD patterns of Fe-NiTe and O_V@Fe-NiTe. (b) Raman spectra of O_V@Fe-NiTe and Fe-NiTe. (c) High resolution XPS Te 3d spectra (M=Ni, Fe) and (d) XPS O 1 s spectra of O_V@Fe-NiTe and Fe-NiTe. (e) XANES Te $M_{2,3}$-edge spectra and (f) XANES O K-edge spectra of O_V@Fe-NiTe and Fe-NiTe.

TeO_2 on the pristine Fe-NiTe. For the XAS O K-edge spectrum displayed in Fig. 3f, the shape-resonances of A and A' at around 533.3 eV are related to oxygen 2p antibonding states hybridized with Te 5p. The shape-resonances marked B and B' at 540.2 eV and 539.6 eV are corresponding to the O 2p-Te 4d hybridization of O_V@Fe-NiTe and pristine Fe-NiTe according to the previous reports [44,45], respectively. The photo energy of the peaks in O K-edge spectrum is related to hybridization strength. The evident shifts of both shape-resonance A and B toward higher photo energy of O_V@Fe-NiTe comparing with that of pristine Fe-NiTe suggests weaker O 2p* -Te 5p and O 2p-Te 4d hybridization strength [46], which confirms the improvement of O_V ratio in O_V@Fe-NiTe.

To unveil the mechanism of the CEA process, we conduct a series of characterizations. We perform the ICP to detect the ion concentration of Ni and Fe in the electrolyte after the CEA process. The ion concentration of Ni and Fe is $3.2 * 10^{-8}$ mol L^{-1} and $1.3 * 10^{-8}$ mol L^{-1}, respectively (Table S1). Therefore, the CEA process does not result in the dissolution of Fe-NiTe. Compared with the evident differences of XPS Te 3d spectra and XAS Te $M_{2,3}$-edge spectrum between O_V@Fe-NiTe and Fe-NiTe, the very tiny changes of XPS Ni 2p spectra, XAS Ni $L_{2,3}$-edge spectrum and XAS Fe $L_{2,3}$-edge spectrum (Fig.S9a-c) demonstrate the mainly substance transformation in the CEA process occurs on the Te site. Thus, in the CEA process, the self-formed TeO_2 on the surface of Fe-NiTe is reduced when a bias of -0.2 V is applied, which promote the generation of oxygen vacancy and make more undercoordinated active Te

terminal exposed. The abundant undercoordinated Te terminal leads to the formation of TeO_2 [24]. As a result, under the continuous bias of -0.2 V, it forms oxygen vacancy-rich TeO_2 layer on the surface of O_V@Fe-NiTe.

3.2. OER performance measurement

We evaluated the intrinsic OER performance of as-prepared materials in 1 M KOH. Fig. 4a illustrates the LSV curves of O_V@Fe-NiTe, pristine Fe-NiTe, commercial RuO_2 and pristine Ni foam with iR compensation. The overpotential of pristine Fe-NiTe to attain a current density of 100 mA cm^{-2} is 340 mV. Interestingly, to drive the same current density, the O_V@Fe-NiTe only requires an overpotential of 245 mV, much lower than that of pristine Fe-NiTe. These results suggest that the CEA process dramatically improves the OER performance. In addition, the poor OER performance of pure Ni foam (335 mV @ 10 mA cm^{-2}) further confirms the favorable intrinsic activity of O_V@Fe-NiTe. To further study the OER reaction kinetics, we calculate the Tafel slope through the following Eq. (1):

$$\eta = b\log(j) + a \tag{7}$$

where b, j and η represents the Tafel slope, current density and overpotential, respectively. Fig. 4b illustrates the Tafel plots of as-prepared catalysts. The Tafel slope value for O_V@Fe-NiTe is 35.5 mV dec^{-1},
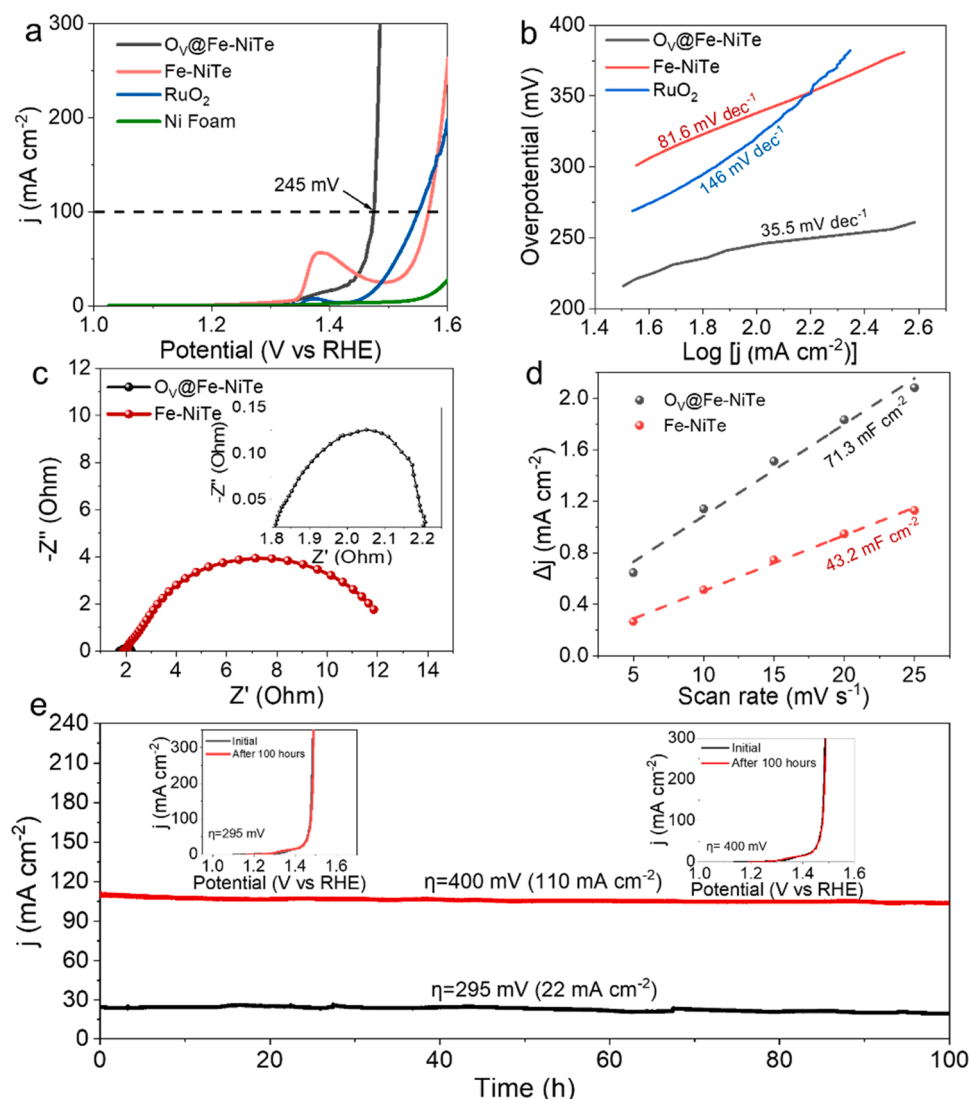
Fig. 4. (a) LSV curves of the O_V@Fe-NiTe, Fe-NiTe, commercial RuO_2 and Ni Foam. (b) Tafel plots of the O_V@Fe-NiTe, Fe-NiTe and commercial RuO_2. (c) EIS Nyquist plots of the as-prepared materials and the EIS Nyquist plots of O_V@Fe-NiTe (inset). (d) Capacitive current density-scan rate plots. (e) Chronoamperometric curves of O_V@Fe-NiTe without iR compensation. The inset: LSV curves before and after 100 h.

lower than Fe-NiTe (81.6 mV dec^{-1}), suggesting fast OER kinetics of O_V@Fe-NiTe. Compared with the commercial RuO_2 (overpotential: 321 mV @ 100 mA cm^{-2}), the O_V@Fe-NiTe also exhibits better OER performance with lower overpotential and faster kinetics (Fig. 4a and b). Remarkably, O_V@Fe-NiTe exhibited the best reported OER performance among recently published transition metal tellurides, as listed in Table S2.

To comprehend the mechanism of OER activity improvement of O_V@Fe-NiTe, we measure the EIS (electrochemical impedance spectra) and ECSA (electrochemical surface area). Fig. 4c depicts the Nyquist plots of Fe-NiTe and O_V@Fe-NiTe, the related equivalent circuit is shown in Fig. S10. According to the equivalent circuit, the Fe-NiTe and O_V@Fe-NiTe possess similar inherent resistance as listed in Table S3. The diameter of semicircle represents the charge transfer resistance (R_{ct}). It could be obviously observed that the R_{ct} of O_V@Fe-NiTe (0.4 Ω) is much smaller than that of Fe-NiTe (10.5 Ω). This observation indicates that optimized electron structure of the activated tellurides expedites electronic transport and Faradic process. The ECSA is positively related to the C_{dl} (electrochemical double layer capacitance) [47,48]. The C_{dl} is investigated by the CV curves as shown in Fig. S6c and S11a. According to Fig. 4d, O_V@Fe-NiTe (71.3 mF cm^{-2}) has the higher C_{dl} value compared with pristine Fe-NiTe (43.2 mF cm^{-2}), which demonstrates
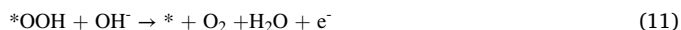
that CEA process can improve the number of active sites. Fig. S11b illustrates the LSV curves normalized to ECSA (Table S4). The overpotential of O_V@Fe-NiTe is lower than not activated counterparts to attain the same current density, proving that the CEA process improve the intrinsic OER property of telluride evidently. The Bode plots of the as-prepared catalysts shown in the Fig. S12a-c reveal a smaller phase angle of O_V@Fe-NiTe at each potential comparing with that of pristine Fe-NiTe. This phenomenon confirms that more electrons participate in the water oxidation, further demonstrating the higher intrinsic OER activity for O_V@Fe-NiTe.

We measured the long-term stability of the O_V@Fe-NiTe by conducting chronoamperometry at an overpotential of 295 mV and 400 mV (without iR correction) for 100 h in 1 M KOH. No obvious decrease of current densities at both the two potentials is detected (Fig. 4e) indicating excellent stability. The LSV curve also displayed negligible change even after 100 h chronoamperometric test (inset of Fig. 4e), further confirming the excellent stability of O_V@Fe-NiTe. In addition, XRD pattern, Raman spectra, SEM and TEM images demonstrated unchanged composition and morphology of the O_V@Fe-NiTe after stability test as shown in Fig. S13 and Fig. S14, supporting the stability of the material under those conditions.

### 3.3. Role of Ov in enhancement of OER performance

To unveil electrocatalytic enhancement mechanism through the CEA method, we further characterized the composition of catalysts after the long-term OER tests. Conventional adsorbate evolution mechanism for OER has been widely accepted, and it involves a four-electron transfer pathway and multiple adsorbed intermediates, as follows:

$$* + OH^- \rightarrow *OH + e^- \tag{8}$$

$$*OH + OH^- \rightarrow *O + H_2O + e^- \tag{9}$$

$$*O + OH^- \rightarrow *OOH + e^- \tag{10}$$

$$*OOH + OH^- \rightarrow * + O_2 + H_2O + e^- \tag{11}$$

in which the * is the active sites, *OH, *O and *OOH are the intermediates in the OER. XPS spectroscopy was performed to characterize the composition after 100 h' chronoamperometric OER test. The O_V@Fe-NiTe and pristine Fe-NiTe have similar chemical state of Ni and Te after OER test (Fig. S15a and b). Interestingly, Fig. 5a presents the O 1 s spectra of O_V@Fe-NiTe and pristine Fe-NiTe after OER test, Fig.6a shows the XPS O 1 s spectra of O_V@Fe-NiTe and Fe-NiTe after 100 h'

OER chronoamperometric test. The deconvoluted peaks at 529.8, 530.6, 531.5, 532.2 and 533.2 eV are corresponding to the *OOH, lattice O, surface O, O_V and the O in adsorbed H2O [49,50]. In the Raman spectra of O_V@Fe-NiTe and Fe-NiTe after OER test (Fig.S14b), the wide peak of O_V@Fe-NiTe around 900 cm^{-1}~1150 cm^{-1} is ascribed to the *OOH [49]. The obtained results of XPS and Raman spectra demonstrate the higher content of *OOH adsorbed on the O_V@Fe-NiTe (13.48%) compared with Fe-NiTe (5.75%). This demonstrates that the formed O_V-rich TeO_2 on the surface of O_V@Fe-NiTe enhance the adsorption of *OOH to achieve the OER activity improvement.

We further investigated the OER mechanism through DFT (Density Functional Theory) calculations. The model Fe-doped NiTe-TeO_2 with O vacancy (Fe-NiTe-TeO_2(O_V)) (Fig. 5b) is constructed according to the above XRD, Raman, XPS and XAS characterization. In addition, Fe-doped NiTe-TeO_2 layer without O vacancies (Fe-NiTe-TeO_2, Fig. S16a) and TeO_2 (Fig. S17a) are also constructed to serve as the contrast models. The computational details are supplied in the experimental section. The OER through adsorbate evolution mechanism pathway on Fe-NiTe-TeO_2(O_V), Fe-NiTe-TeO_2 and TeO_2 and the corresponding intermediate adsorption configurations are shown in the Fig. 5c, Fig. S16b and Fig. S17b, respectively. According to the free energy diagram (U = 0 V) of the above three models (Fig. 5d), the ΔG_{Max} (maximum of free
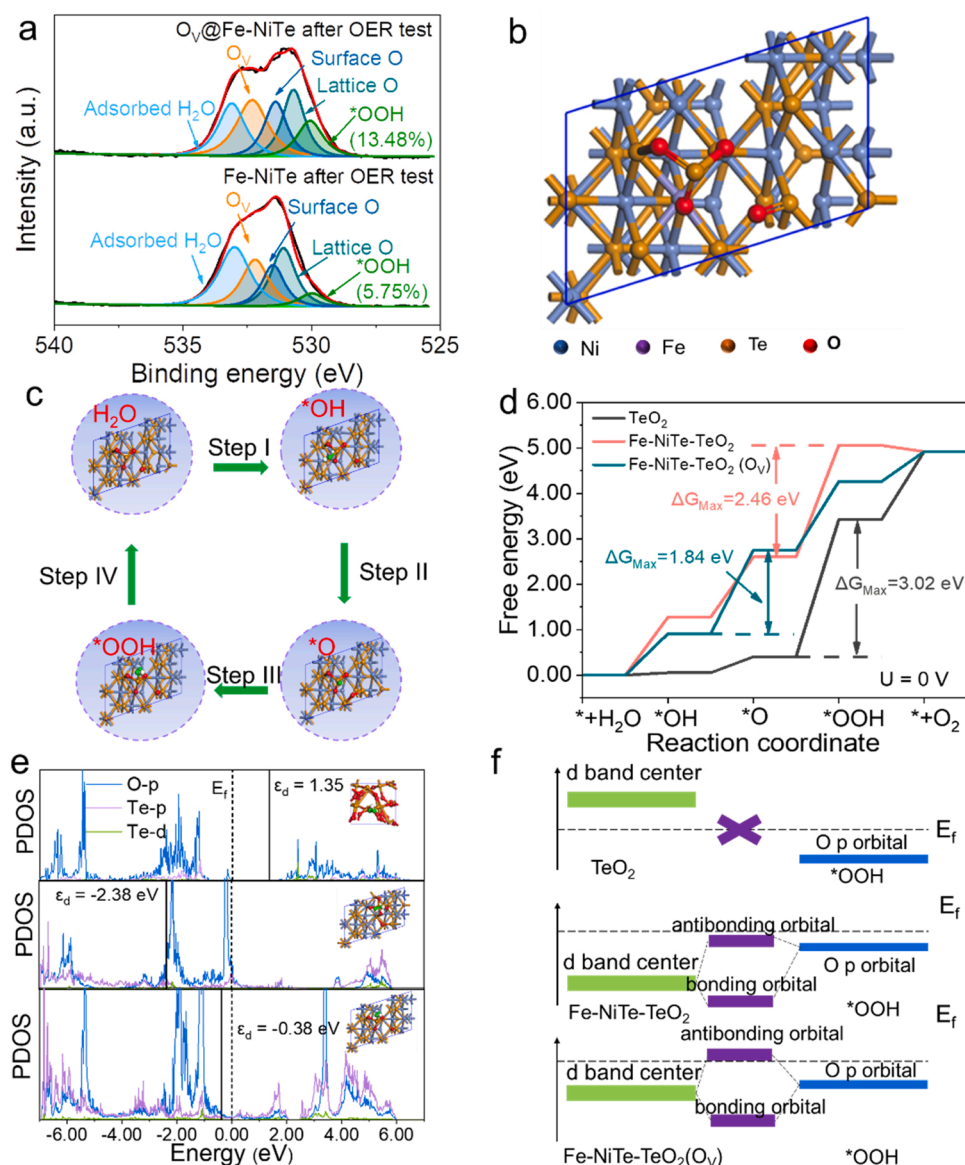
Fig. 5. (a) High resolution XPS O 1 s spectra of Fe-NiTe and O_V@Fe-NiTe after 100 h' Chronoamperometric test. (b) Simulated Fe-NiTe-TeO_2(O_V) model. (c) The OER reaction pathway of the Fe-NiTe-TeO_2(O_V). (d)The reaction free diagram on Fe-NiTe-TeO_2, Fe-NiTe-TeO_2(O_V) and TeO_2 model (U=0) for OER. (e) The Projected electronic densities of states of TeO_2-OOH (first graph), Fe-NiTe-TeO_2-OOH (second graph) and Fe-NiTe-TeO_2(O_V)-OOH (third graph). (f) The interaction of D-band center of the Fe-NiTe-TeO_2, Fe-NiTe-TeO_2(O_V) and TeO_2 model with the O p orbital of *OOH.

energy difference) of Fe-NiTe-TeO$_2$ (O$_V$) (1.84 eV) is much lower than that of Fe-NiTe-TeO$_2$ (2.46 eV) and pristine TeO$_2$ model (3.02 eV), indicating a higher OER activity of the Fe-NiTe-TeO$_2$ (O$_V$), which is consistent with the experimental results. Further calculations at 1.23 V (Fig. S18a) indicated a lower overpotential of Fe-NiTe-TeO$_2$ (O$_V$) (0.61 V). Particularly, the potential determining step (PDS) of the Fe-NiTe-TeO$_2$ (O$_V$) is the deprotonation of the *OH intermediate, while that of the Fe-NiTe-TeO$_2$ and TeO$_2$ is the formation of the *OOH intermediate. Further investigation of the adsorption energy of *OOH (Fig. S18b) indicated a higher *OOH adsorption capacity of Fe-NiTe-TeO$_2$(O$_V$), which is consistent with the XPS result (Fig. 5a). These observations suggest that oxygen vacancies in the Fe-NiTe-TeO$_2$(O$_V$) could facilitate the formation of *OOH and hence, enhance its OER catalytic activity.

According to the previous theoretical study, the adsorption energy from the active sites to the intermediates is decided by the D-states of the active sites [51]. The ε_d of the pristine TeO$_2$, Fe-NiTe-TeO$_2$ and Fe-Ni-Te-TeO$_2$(O$_V$) are 1.35, $-$ 2.38 and $-$ 0.38 eV, respectively (Fig. S19). The PDOS (projected density of states) of *OOH adsorption on above models (Fig. 5e) were studied to elucidate the interaction between intermediate and active sites involved in the related mechanism. Fig. 5f shows the schematic diagram of the interaction of D-band center of the three models with the O p orbital of *OOH. For the TeO$_2$, the ε_d locals above the E$_F$, which could not hybridize with the O p orbital of *OOH, resulting in a low *OOH adsorption capacity of the pristine TeO$_2$. In contrast, the ε_d of the Fe-NiTe-TeO$_2$ and the Fe-NiTe-TeO$_2$ (O$_V$) both locate under the E$_F$ and will form effective hybridized orbitals with *OOH. The hybridized orbitals would split into bonding orbital and antibonding orbital. Regarding the Fe-NiTe-TeO$_2$, both the bonding orbitals and antibonding orbital are under the Fermi level. For the Fe-NiTe-TeO$_2$ (O$_V$), interestingly, ε_d is closer to the Fermi level compared with that of Fe-NiTe-TeO$_2$; and the antibonding orbital localizes above the E$_F$, thus leading to less electrons filling in the antibonding orbital of Fe-NiTe-TeO$_2$(O$_V$), which is beneficial in enhancing interaction with *OOH. Furthermore, Tang's recent work proves that the oxygen vacancy in reconstruction layer on NiCo-MOF promotes the formation of *OOH through in-situ characterization [52]. Similarly, the oxygen vacancy in the Fe-NiTe-TeO$_2$ (O$_V$) raises D-band center of active Te atom, leading to the antibonding orbital exceeds the Fermi level. As a result, the *OOH adsorption has been enhanced, and OER pathway is further optimized to achieve better OER performance.

4. Conclusion

In summary, a unique in-situ cathodic electrochemical activation was employed to facilitate the surface self-reconstruction to form O$_V$-rich TeO$_2$ layer on the Fe-NiTe. Interestingly, in 1 M KOH, the as-prepared O$_V$@Fe-NiTe exhibited remarkable OER electrocatalytic activity, along with ultralow overpotential of 245 mV at 100 mA cm^{-2} and fast kinetics, exhibiting great stability, too. Moreover, characterizations and theoretical calculation suggest that the formation of O$_V$-rich TeO$_2$ layer onto Fe-NiTe facilitates the movement of D-band center of active Te to optimize splitting orbital, which promotes *OOH adsorption and hence, enhances the OER performance. This work identifies for the first time the OER mechanism of the TeO$_2$ layer on Fe-NiTe and provides a novel avenue to exploit this type of low-cost electrocatalysts through electrochemical surface engineering.

CRediT authorship contribution statement

Peng Guo: Methodology, Investigation, Writing – original draft. **Shoufu Cao:** Software, Visualization. **Yijin Wang:** Formal analysis, Validation. **Xiaoqing Lu:** Software, Visualization. **Youzi Zhang:** Validation. **Xu Xin:** Validation. **Xiao Chi:** Data curation. **Xiaojiang Yu:** Data curation. **Ilhom Tojiboyev:** Writing – review & editing. **Hadi Salari:** Writing – review & editing. **Ana Jorge Sobrido:** Data curation.

Magdalena Titirici: Writing – review & editing. **Xuanhua Li:** Resources, Funding acquisition, Supervision.

Declaration of Competing Interest

The authors declare that they have no known competing financial interests or personal relationships that could have appeared to influence the work reported in this paper.

Appendix A. Supporting information

Supplementary data associated with this article can be found in the online version at doi:10.1016/j.apcatb.2022.121355.

References

[1] C. Liu, J. Qian, Y. Ye, H. Zhou, C.-J. Sun, C. Sheehan, Z. Zhang, G. Wan, Y.-S. Liu, J. Guo, S. Li, H. Shin, S. Hwang, T.B. Gunnoe, W.A. Goddard III, S. Zhang, Oxygen evolution reaction over catalytic single-site Co in a well-defined brookite TiO2 nanorod surface, Nat. Catal. 4 (2021) 36–45, https://doi.org/10.1038/s41929-020-00550-5.

[2] J. Hwang, R.R. Rao, L. Giordano, Y. Katayama, Y. Yu, Y. Shao-Horn, Perovskites in catalysis and electrocatalysis, Science 358 (2017) 751–756, https://doi.org/10.1126/science.aam7092.

[3] T. Wu, X. Ren, Y. Sun, S. Sun, G. Xian, G.G. Scherer, A.C. Fisher, D. Mandler, J. W. Ager, A. Grimaud, J. Wang, C. Shen, H. Yang, J. Gracia, H.-J. Gao, Z.J. Xu, Spin pinning effect to reconstructed oxyhydroxide layer on ferromagnetic oxides for enhanced water oxidation, Nat. Commun. 12 (2021) 3634, https://doi.org/10.1038/s41467-021-23896-1.

[4] W.H. Lee, N. Hong Nhan, C.H. Choi, K.H. Chae, Y.J. Hwang, B.K. Min, P. Strasser, H.-S. Oh, Carbon-supported IrCoOx nanoparticles as an efficient and stable OER electrocatalyst for practicable CO$_2$ electrolysis, Appl. Catal. B Environ. 269 (2020), 118820, https://doi.org/10.1016/j.apcatb.2020.118820.

[5] Y. Liu, C. Ma, Q. Zhang, W. Wang, P. Pan, L. Gu, D. Xu, J. Bao, Z. Dai, 2D electron gas and oxygen vacancy induced high oxygen evolution performances for advanced Co3O4/CeO2 nanohybrids, Adv. Mater. 31 (2019), 1900062, https://doi.org/10.1002/adma.201900062.

[6] T. Wu, S. Sun, J. Song, S. Xi, Y. Du, B. Chen, W.A. Sasangka, H. Liao, C.L. Gan, G. G. Scherer, L. Zeng, H. Wang, H. Li, A. Grimaud, Z.J. Xu, Iron-facilitated dynamic active-site generation on spinel CoAl2O4 with self-termination of surface reconstruction for water oxidation, Nat. Catal. 2 (2019) 763–772, https://doi.org/10.1038/s41929-019-0325-4.

[7] Y. Pan, X. Xu, Y. Zhong, L. Ge, Y. Chen, J.-P.M. Veder, D. Guan, R. O'Hayre, M. Li, G. Wang, H. Wang, W. Zhou, Z. Shao, Direct evidence of boosted oxygen evolution over perovskite by enhanced lattice oxygen participation, Nat. Commun. 11 (2020) 2002, https://doi.org/10.1038/s41467-020-15873-x.

[8] H. Kim, J. Kim, J. Kim, G.H. Han, W. Guo, S. Hong, H.S. Park, H.W. Jang, S.Y. Kim, S.H. Ahn, Dendritic gold-supported iridium/iridium oxide ultra-low loading electrodes for high-performance proton exchange membrane water electrolyzer, Appl. Catal. B Environ. 283 (2021) 119596, https://doi.org/10.1016/j.apcatb.2020.119596.

[9] P. Zhai, Y. Zhang, Y. Wu, J. Gao, B. Zhang, S. Cao, Y. Zhang, Z. Li, L. Sun, J. Hou, Engineering active sites on hierarchical transition bimetal oxides/sulfides heterostructure array enabling robust overall water splitting, Nat. Commun. 11 (2020), https://doi.org/10.1038/s41467-020-19214-w.

[10] H. Su, S. Song, S. Li, Y. Gao, L. Ge, W. Song, T. Ma, J. Liu, High-valent bimetal Ni3S2/Co3S4 induced by Cu doping for bifunctional electrocatalytic water splitting, Appl. Catal. B Environ. 293 (2021), 120225, https://doi.org/10.1016/j.apcatb.2021.120225.

[11] Z. Fang, L. Peng, H. Lv, Y. Zhu, C. Yan, S. Wang, P. Kalyani, X. Wu, G. Yu, Metallic transition metal selenide holey nanosheets for efficient oxygen evolution electrocatalysis, ACS Nano 11 (2017) 9550–9557, https://doi.org/10.1021/acsnano.7b05481.

[12] J. Huang, S. Wen, G. Chen, W. Chen, G. Wang, H. Fan, D. Chen, C. Song, M. Li, X. Wang, L. Li, M. Tao, B. Li, X. Wang, K. Ostrikov, Multiphase Ni-Fe-selenide

nanosheets for highly-efficient and ultra-stable water electrolysis, Appl. Catal. B Environ. 277 (2020), 119220, https://doi.org/10.1016/j.apcatb.2020.119220.

[13] U. De Silva, J. Masud, N. Zhang, Y. Hong, W.P.R. Liyanage, M.A. Zaeem, M. Nath, Nickel telluride as a bifunctional electrocatalyst for efficient water splitting in alkaline medium, J. Mater. Chem. A 6 (2018) 7608–7622, https://doi.org/10.1039/c8ta01760c.

[14] Q. Gao, C.-Q. Huang, Y.-M. Ju, M.-R. Gao, J.-W. Liu, D. An, C.-H. Cui, Y.-R. Zheng, W.-X. Li, S.-H. Yu, Phase-selective syntheses of cobalt telluride nanofleeces for efficient oxygen evolution catalysts, Angew. Chem. Int. Ed. 56 (2017) 7769–7773, https://doi.org/10.1002/anie.201701998.

[15] M. Sadaqat, L. Nisar, N.-U.-A. Babar, F. Hussain, M.N. Ashiq, A. Shah, M.F. Ehsan, M. Najam-Ul-Haq, K.S. Joya, Zinc-telluride nanospheres as an efficient water oxidation electrocatalyst displaying a low overpotential for oxygen evolution, J. Mater. Chem. A 7 (2019) 26410–26420, https://doi.org/10.1039/c9ta07171g.

[16] Z. Chen, M. Chen, X. Yan, H. Jia, B. Fei, Y. Ha, H. Qing, H. Yang, M. Liu, R. Wu, Vacancy occupation-driven polymorphic transformation in cobalt ditelluride for boosted oxygen evolution reaction, ACS Nano 14 (2020) 6968–6979, https://doi.org/10.1021/acsnano.0c01456.

[17] Z. Xue, X. Li, Q. Liu, M. Cai, K. Liu, M. Liu, Z. Ke, X. Liu, G. Li, Interfacial electronic structure modulation of NiTe nanoarrays with NiS nanodots facilitates electrocatalytic oxygen evolution, Adv. Mater. 31 (2019), 1900430, https://doi.org/10.1002/adma.201900430.

[18] H. Sun, J.-M. Yang, J.-G. Li, Z. Li, X. Ao, Y.-Z. Liu, Y. Zhang, Y. Li, C. Wang, J. Tang, Synergistic coupling of NiTe nanoarrays with RuO2 and NiFe-LDH layers for high-efficiency electrochemical-/photovoltage-driven overall water splitting, Appl. Catal. B Environ. 272 (2020), 118988, https://doi.org/10.1016/j.apcatb.2020.118988.

[19] L. Hu, X. Zeng, X. Wei, H. Wang, Y. Wu, W. Gu, L. Shi, C. Zhu, Interface engineering for enhancing electrocatalytic oxygen evolution of NiFe LDH/NiTe heterostructures, Appl. Catal. B Environ. 273 (2020), 119014, https://doi.org/10.1016/j.apcatb.2020.119014.

[20] J. Wang, L. Han, B. Huang, Q. Shao, H.L. Xin, X. Huang, Amorphization activated ruthenium-tellurium nanorods for efficient water splitting, Nat. Commun. 10 (2019) 5692, https://doi.org/10.1038/s41467-019-13519-1.

[21] B. Tang, X. Yang, Z. Kang, L. Feng, Crystallized RuTe2 as unexpected bifunctional catalyst for overall water splitting, Appl. Catal. B Environ. 278 (2020), 119281, https://doi.org/10.1016/j.apcatb.2020.119281.

[22] M. Liu, X. Lu, C. Guo, Z. Wang, Y. Li, Y. Lin, Y. Zhou, S. Wang, J. Zhang, Architecting a mesoporous N-doped graphitic carbon framework encapsulating CoTe2 as an efficient oxygen evolution electrocatalyst, ACS Appl. Mater. Interfaces 9 (2017) 36146–36153, https://doi.org/10.1021/acsami.7b09897.

[23] L. Tao, M. Huang, S. Guo, Q. Wang, M. Li, X. Xiao, G. Cao, Y. Shao, Y. Shen, Y. Fu, M. Wang, Surface modification of NiCo2Te4 nanoclusters: a highly efficient electrocatalyst for overall water-splitting in neutral solution, Appl. Catal. B Environ. 254 (2019) 424–431, https://doi.org/10.1016/j.apcatb.2019.05.010.

[24] S. Nappini, D.W. Boukhvalov, G. D'Olimpio, L. Zhang, B. Ghosh, C.-N. Kuo, H. Zhu, J. Cheng, M. Nardone, L. Ottaviano, D. Mondal, R. Edla, J. Fuji, C.S. Lue, I. Vobornik, J.A. Yarmoff, A. Agarwal, L. Wang, L. Zhang, F. Bondino, A. Politano, Transition-metal dichalcogenide NiTe2: an ambient-stable material for catalysis and nanoelectronics, Adv. Funct. Mater. 30 (2020), 2000915, https://doi.org/10.1002/adfm.202000915.

[25] G. D'Olimpio, C. Guo, C.-N. Kuo, R. Edla, C.S. Lue, L. Ottaviano, P. Torelli, L. Wang, D.W. Boukhvalov, A. Politano, PdTe2 transition-metal dichalcogenide: chemical reactivity, thermal stability, and device implementation, Adv. Funct. Mater. 30 (2020), 1906556, https://doi.org/10.1002/201906556.

[26] L. Zhong, Y. Bao, X. Yu, L. Feng, An Fe-doped NiTe bulk crystal as a robust catalyst for the electrochemical oxygen evolution reaction, Chem. Commun. 55 (2019) 9347–9350, https://doi.org/10.1039/c9cc04429a.

[27] L. Zhong, Y. Bao, L. Feng, Fe-doping effect on CoTe catalyst with greatly boosted intrinsic activity for electrocatalytic oxygen evolution reaction, Electrochim. Acta 321 (2019), 134656, https://doi.org/10.1016/j.electacta.2019.134656.

[28] G. Kresse, J. Furthmuller, Efficient iterative schemes for ab initio total-energy calculations using a plane-wave basis set, Phys. Rev. B 54 (1996) 11169–11186, https://doi.org/10.1103/PhysRevB.54.11169.

[29] J.P. Perdew, K. Burke, M. Ernzerhof, Generalized gradient approximation made simple, Phys. Rev. Lett. 78 (1997), https://doi.org/10.1103/PhysRevLett.77.3865.

[30] K. Mathew, R. Sundararaman, K. Letchworth-Weaver, T.A. Arias, R.G. Hennig, Implicit solvation model for density-functional study of nanocrystal surfaces and reaction pathways, J. Chem. Phys. 140 (2014), https://doi.org/10.1063/1.4865107.

[31] J.K. Norskov, J. Rossmeisl, A. Logadottir, L. Lindqvist, J.R. Kitchin, T. Bligaard, H. Jonsson, Origin of the overpotential for oxygen reduction at a fuel-cell cathode, J. Phys. Chem. B 108 (2004) 17886–17892, https://doi.org/10.1021/jp047349j.

[32] X. Chia, A. Ambrosi, Z. Sofer, J. Luxa, M. Pumera, Catalytic and charge transfer properties of transition metal dichalcogenides arising from electrochemical

[33] B. Qin, Y. Bai, Y. Zhou, J. Liu, X. Xie, W. Zheng, Structure and characterization of TeO2 nanoparticles prepared in acid medium, Mater. Lett. 63 (2009) 1949–1951, https://doi.org/10.1016/j.matlet.2009.06.018.

[34] J. Tu, M. Wang, Y. Luo, S. Jiao, Coral-Like TeO2 microwires for rechargeable aluminum batteries, ACS Sustain. Chem. Eng. 8 (2020) 2416–2422, https://doi.org/10.1021/acssuschemeng.9b06193.

[35] E.R. Barney, A.C. Hannon, D. Holland, N. Umesaki, M. Tatsumisago, R.G. Orman, S. Feller, Terminal oxygens in amorphous TeO2, J. Phys. Chem. Lett. 4 (2013) 2312–2316, https://doi.org/10.1021/jz4010637.

[36] T. Sekiya, N. Mochida, A. Ohtsuka, M. Tonokawa, Nippon seramikkusu kyokai gakujutsu ronbunshi, normal vibrations of two polymorphic forms of teo2 crystals and assignments of Raman peaks of pure TeO2 glass, J. Ceram. Soc. Jpn. 97 (1989) 1435–1440, https://doi.org/10.2109/jcersj.97.1435.

[37] S. Babar, P.J. Sellin, J.F. Watts, M.A. Baker, An XPS study of bromine in methanol etching and hydrogen peroxide passivation treatments for cadmium zinc telluride radiation detectors, Appl. Surf. Sci. 264 (2013) 681–686, https://doi.org/10.1016/j.apsusc.2012.10.095.

[38] L. Ji, Z. Wang, H. Wang, X. Shi, A.M. Asiri, X. Sun, Hierarchical CoTe2 nanowire array: an effective oxygen evolution catalyst in alkaline media, ACS Sustain. Chem. Eng. 6 (2018) 4481–4485, https://doi.org/10.1021/acssuschemeng.7b04309.

[39] Z.-F. Huang, J. Song, Y. Du, S. Xi, S. Dou, J.M.V. Nsanzimana, C. Wang, Z.J. Xu, X. Wang, Chemical and structural origin of lattice oxygen oxidation in Co-Zn oxyhydroxide oxygen evolution electrocatalysts, Nat. Energy 4 (2019) 329–338, https://doi.org/10.1038/s41560-019-0355-9.

[40] M. Baek, D. Kim, K. Yong, Simple but effective way to enhance photoelectrochemical solar-water-splitting performance of ZnO nanorod arrays: charge-trapping Zn(OH)(2) annihilation and oxygen vacancy generation by vacuum annealing, ACS Appl. Mater. Interfaces 9 (2017) 2317–2325, https://doi.org/10.1021/acsami.6b12555.

[41] Y. Liu, C. Ma, Q. Zhang, W. Wang, P. Pan, L. Gu, D. Xu, J. Bao, Z. Dai, 2D electron gas and oxygen vacancy induced high oxygen evolution performances for advanced Co3O4/CeO2 nanohybrids, Adv. Mater. 31 (2019), 201900062, https://doi.org/10.1002/adma.201900062.

[42] C. Zhang, X. Geng, J. Li, Y. Luo, P. Lu, Role of oxygen vacancy in tuning of optical, electrical and NO2 sensing properties of ZnO1-x coatings at room temperature, Sens. Actuators, B 248 (2017) 886–893, https://doi.org/10.1016/j.snb.2017.01.105.

[43] L. Wu, J. Hong, Q. Zhang, B.-Y. Chen, J. Wang, Z. Dong, Deciphering highly resistant characteristics to different pHs of oxygen vacancy-rich Fe2Co1-LDH/PS system for bisphenol A degradation, Chem. Eng. J. 385 (2020), 123620, https://doi.org/10.1016/j.cej.2019.123620.

[44] F. Frati, M.F.M. de Groot, Oxygen K-edge X-ray absorption spectra, Chem. Rev. 120 (2020) 4056–4110, https://doi.org/10.1021/acs.chemrev.9b00439.

[45] N. Jiang, J.C.H. Spence, Modeling core-hole effects in electron energy-loss spectroscopy of TeO2, Phys. Rev. B 70 (2004), https://doi.org/10.1103/PhysRevB.70.014112.

[46] N. Palina, A. Annadi, T.C. Asmara, C. Diao, X. Yu, M.B.H. Breese, T. Venkatesan, Ariando, A. Rusydi, Electronic defect states at the LaAlO3/SrTiO3 heterointerface revealed by O K-edge X-ray absorption spectroscopy, Phys. Chem. Chem. Phys. 18 (2016) 13844–13851, https://doi.org/10.1039/c6cp00028b.

[47] S. Li, S. Sirisomboonchai, A. Yoshida, X. An, X. Hao, A. Abudula, G. Guan, Bifunctional CoNi/CoFe2O4/Ni foam electrodes for efficient overall water splitting at a high current density, J. Mater. Chem. A 6 (2018) 19221–19230, https://doi.org/10.1039/c8ta08223e.

[48] Q. Zhang, W. Chen, G. Chen, J. Huang, C. Song, S. Chu, R. Zhang, G. Wang, C. Li, K. K. Ostrikov, Bi-metallic nitroxide nanodot-decorated tri-metallic sulphide nanosheets by on-electrode plasma-hydrothermal sprouting for overall water splitting, Appl. Catal. B Environ. 261 (2020), 118254, https://doi.org/10.1016/j.apcatb.2019.118254.

[49] Q. Xu, M. Chu, M. Liu, J. Zhang, H. Jiang, C. Li, Fluorine-triggered surface reconstruction of Ni3S2 electrocatalysts towards enhanced water oxidation, Chem. Eng. J. 411 (2021), 128488, https://doi.org/10.1016/j.cej.2021.128488.

[50] H. Zhang, H. Jiang, Q. Xu, Y. Hu, C. Li, Rapid low-temperature synthesis of hollow CuS0.55 nanoparticles for efficient electrocatalytic water oxidation, Chem. Eng. Sci. 195 (2019) 665–670, https://doi.org/10.1016/j.ces.2018.10.011.

[51] S. Wang, H.S. Pillai, H. Xin, Bayesian learning of chemisorption for bridging the complexity of electronic descriptors, Nat. Commun. 11 (2020) 6132, https://doi.org/10.1038/s41467-020-19524-z.

[52] S.L. Zhao, C.H. Tan, C.T. He, P.F. An, F. Xie, S. Jiang, Y.F. Zhu, K.H. Wu, B. W. Zhang, H.J. Li, J. Zhang, Y. Chen, S.Q. Liu, J.C. Dong, Z.Y. Tang, Structural transformation of highly active metal-organic framework electrocatalysts during the oxygen evolution reaction, Nat. Energy 5 (2020) 881–890, https://doi.org/10.1038/s41560-020-00709-1.